

Fine Resolution Photonic Spectral Processor Using a Waveguide Grating Router With Permanent Phase Trimming

Noam Goldshtein, David Sinefeld, Ori Golani, Roy Rudnick, Leonid Pascar, Roy Zektzer, and Dan M. Marom, *Senior Member, IEEE, Fellow, OSA*

(*Top-Scoring Paper*)

Abstract—Spectrally dispersed light from a fine resolution waveguide grating router (WGR) of 25-GHz free spectral range that radiates to free space is spatially filtered at ~ 1 GHz optical resolution and 50 MHz spectral addressability using a liquid crystal on Silicon (LCoS) spatial light modulator (SLM). Fabrication imperfections leading to phase errors on the 32 waveguide arms of the WGR are corrected using a UV pulsed laser to inscribe permanent optical path changes to the waveguides. WGR phase errors are permanently trimmed waveguide-by-waveguide with an excimer laser by inducing stress in the glass cladding above the waveguide for coarse setting and using the photosensitivity effect for fine setting. The WGR was then mated with an LCoS SLM located at the Fourier plane to form a photonic spectral processor, for arbitrary spectral amplitude and phase manipulations.

Index Terms—Optical communication, optical filters, optical planar waveguide components, optical waveguide components, wavelength division multiplexing.

I. INTRODUCTION

PLANAR lightwave circuit (PLC) waveguide grating router (WGR) based systems are commonly used in modern optical communications, mainly as multiplexers and demultiplexers. A special class of spectral processing devices uses a unique WGR design with unconventional output; instead of employing a second slab-lens region that demultiplexes to individual output waveguides, the grating arms terminate at the PLC edge and the light radiates to free-space, forming a phased array exhibiting angular dispersion. The diffracted, angularly dispersed light is converted by a Fourier lens to spatially dispersed light at the lens back focal plane, where it may be manipulated by a spatial light modulator (SLM), employing either MEMS micromirrors [1], [2] or liquid crystal on Silicon (LCoS) pixels [3], [4] (see Fig. 1). Such hybrid guided-wave/free-space optics processors can serve as a more compact realization of a wavelength-selective switch

Manuscript received July 20, 2015; revised October 6, 2015; accepted November 15, 2015. Date of publication December 16, 2015; date of current version February 5, 2016. This work was supported in part by the EC FP7-ICT project FOX-C under Grant 318415, the EU-FP7 PianoPlus project OTONES, and the TeraSanta program of the Israel Ministry of Economics.

The authors are with the Applied Physics Department, The Hebrew University, Jerusalem 91904, Israel (e-mail: noam.goldshtein@mail.huji.ac.il; sinefeld@gmail.com; ori.golani@mail.huji.ac.il; roi.rudnick@gmail.com; leonid.pascar@mail.huji.ac.il; roy.zektzer@mail.huji.ac.il; danmarom@mail.huji.ac.il).

Color versions of one or more of the figures in this paper are available online at <http://ieeexplore.ieee.org>.

Digital Object Identifier 10.1109/JLT.2015.2508450

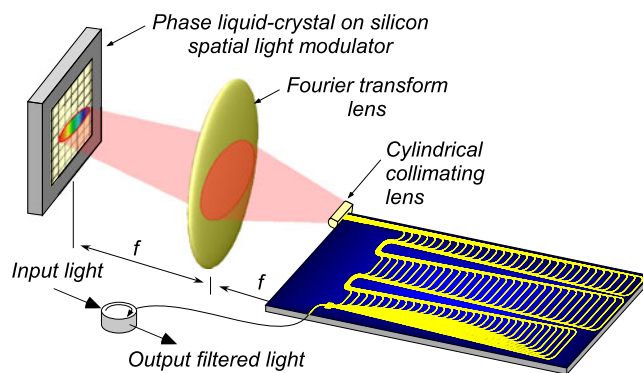


Fig. 1. Hybrid guided-wave/free-space optics dispersive platform with LCoS SLM for spectral manipulation.

than a conventional bulk grating design [5], [6]. The WGR-based dispersive optics further provide a wider design space that can achieve finer optical resolving power, enabling intra-channel spectral filtering applications [7]–[9], giving the fine filtering apparatus the moniker *photonic spectral processor* (PSP).

WGR-based components critically depend on the phase accuracy of the embedded waveguide array [10], yet measuring these phase errors in components such as multiplexers is not trivial as the measurement is indirect [11]. This becomes especially challenging for fine resolution WGR based devices, as the waveguide path length difference increases. A 1 GHz spaced demultiplexer operating over 16 GHz free spectral range (FSR) had to employ waveguide trimming in order to correct for phase errors [12]. Recently we reported the highest resolution PSP based on a WGR with sub-1 GHz optical resolution spanning 200 GHz FSR [13]. The fabricated WGR suffered from phase errors rendering the device inoperable unless the phase errors were corrected. In [13] we employed a dual LCoS approach for addressing this, one for correcting the phase of the WGR output and the second for spectral manipulation of the dispersed and well resolved spectral components.

Here we expand on our conference report on a PSP employing a WGR for fine resolution spectral separation, where a permanent phase trimming technique to the WGR has been directly applied with an excimer laser, correcting for the fabrication phase errors [14]. The optical setup is thus greatly simplified compared to the dual LCoS approach and simply consists of the trimmed WGR, a Fourier lens and single LCoS SLM for

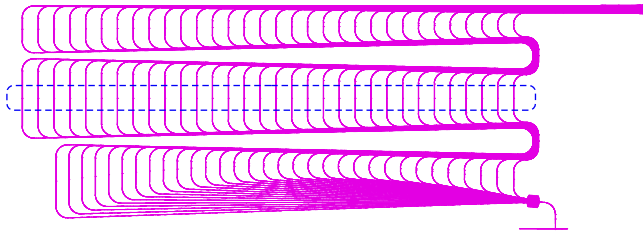


Fig. 2. WGR with sub-1 GHz optical resolution design layout (dimensions $\sim 2 \times 5.5$ cm). Dashed line indicates designed trimming zone, where parallel waveguides are well separated and a few mm long.

spectral manipulations (see Fig. 1). The trimmed WGR used in this experiment has a 25 GHz FSR, and is intended to serve as fine WDM interleaver (12.5/25 GHz) of an OFDM-PON network project [15].

II. WGR DESIGN

A conventional WGR employs a first star coupler (free space region) allowing an input waveguide to radiate into the waveguide array, followed by a second star coupler where the dispersed light emerging from the waveguide array is coupled to individual demultiplexed output waveguides. The WGR we use is unconventional—we discard the second slab lens region that demultiplexes to output waveguides. The grating arms terminate at the PLC edge, allowing the light to radiate into free space. This forms a phased-array output that experiences angular dispersion on account of wavelength-dependent phase delays in the waveguide array. Using an external Fourier lens, we obtain spatially dispersed light allowing for manipulation in free space with an SLM as shown in Fig. 1.

The key design features of a WGR are its incremental path length increase, ΔL , between successive waveguides and number of waveguides, N , within the array. The former sets the FSR according to $\Delta\nu_{\text{FSR}} = c/(n_g \cdot \Delta L)$ (where n_g is the group index of the waveguide propagating mode and c is the speed of light) and the latter sets the spectral resolution $\nu_{\text{res}} \cong \Delta\nu_{\text{FSR}}/N$. The WGR we discuss here is designed to provide fine resolution by limiting the overall bandwidth to a 25 GHz FSR (small $\Delta\nu_{\text{FSR}}$). It was fabricated with $N = 32$ waveguide arms with a relative path length of $\Delta L = m \cdot \lambda_0/n_{\text{eff}} \approx 8$ mm (where $m = 7480$ is the diffraction order and n_{eff} is the waveguide effective index), for a total WGR path length difference of $N \cdot \Delta L \sim 250$ mm. The inverse of the time delay ($\Delta t = N \cdot \Delta L/v_g = 1.25$ ns) matches our 0.8 GHz target resolution, in line with time-bandwidth uncertainty principle. The WGR was implemented in a silica on silicon platform with 2% index contrast waveguides of 4×4 μm cross-section (see Fig. 2) with $n_{\text{eff}} \cong 1.46$. To obtain a compact WGR design for such a long path difference, the waveguides are folded three times within the PLC (total size is 2×5.5 cm). The waveguide pitch at the output (at the PLC edge) is 18.6 μm , and the waveguides are adiabatically broadened to size $\Delta_{\text{wg}} = 17$ μm .

The challenge in realizing such WGR is maintaining the phase accuracy across the entire array, as phase errors will at first lower

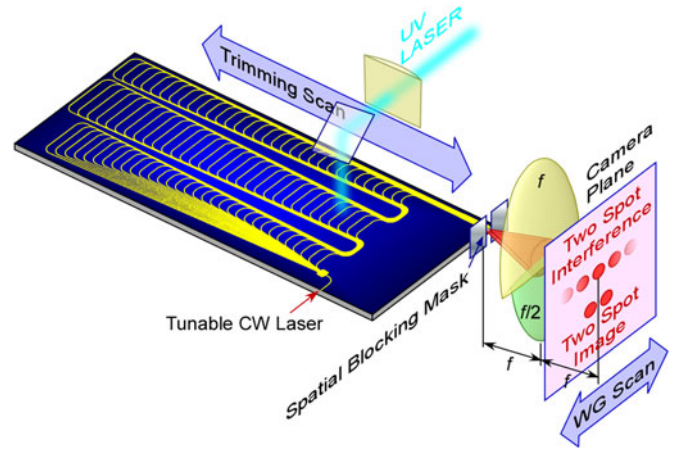


Fig. 3. Layout of the WGR phase errors evaluation and UV trimming system. A slit placed at the WGR output selects two adjacent waveguides whose output is split into two vertical sections, both imaged onto the same IR camera. The upper part is incident on a Fourier lens to form an interference pattern containing the phase error information, and the lower part is imaged for centering the slit on the WG pair. The UV beam individually irradiates the waveguide arms to a dose required to adjust the output phase.

the resolution and then completely ruin the WGR performance if approaching or exceeding π . Many factors may contribute to the sources of phase errors, such as lithography/etching errors, core layer thickness variations, refractive index inhomogeneity and/or stress.

III. PHASE ERROR MEASUREMENT AND ITS COMPENSATION

Our WGR with a radiating output allows direct access to the waveguides at the output facet, in contrast to fully integrated multiplexers. This allows us to devise a direct phase measurement technique, rather than relying on Fourier transform spectroscopy techniques and their associated sensitivity to noise impacting the calculations [11]. In order to obtain phase error information, we block the output facet of the WGR with a spatial mask which contains a slit wide enough to span two adjacent waveguides. The light that emerges from the mask is split in the vertical direction, with one part being imaged and the other Fourier transformed—both onto a single IR camera (see Fig. 3). The former is used to position the mask, moving it relative to the WGR until two equal spots are imaged onto the camera. This ensures us that only two waveguides contribute to the formed interference pattern. The radiating light from the two waveguides interferes in the far field, resulting in an interference pattern that depends on the relative phase between the two waveguides. The phase difference between the two waveguides under test can be obtained by the interference fringe shift. (This is identical to Young's double slit diffraction pattern.) Scanning along all the output waveguides provides the relative phase between each pair of waveguides.

From a single interference image it is difficult to obtain a high fidelity measurement of the phase difference. Hence, we use an additional degree of freedom at our disposal, tuning the interrogating monochromatic laser wavelength exciting the waveguide array. Since the WGR has an incremental length difference between every two waveguides, scanning the wavelength across

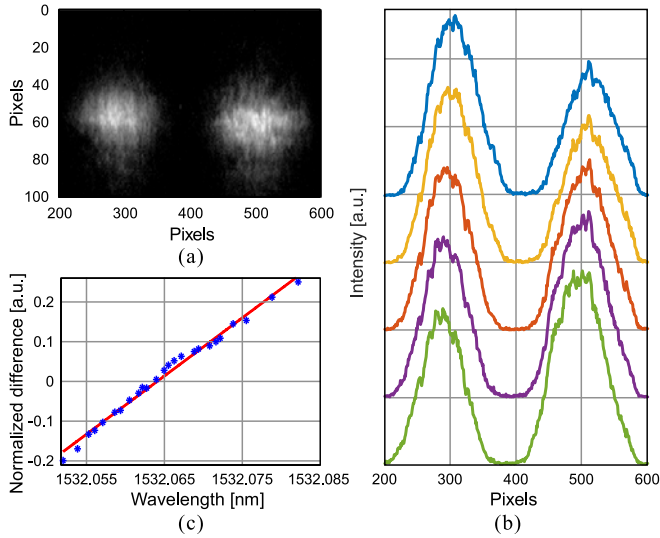


Fig. 4. Wavelength sweep algorithm. (a) Image of far-field interference pattern at the Fourier plane, near equal peaks condition. (b) Lobe intensities extracted from images for different wavelength excitation, as part of wavelength sweep algorithm. (c) Normalized peak difference plotted as a function of wavelength during the scan. From the linear fit of the scanning results λ_{eq} is extracted.

the WGR FSR is identical to adding a phase modulation on the longer waveguide that we can tune at will. When the two waveguides radiate in phase, the far-field interference pattern results in the formation of one major lobe in the far field under the envelope of the individual waveguide far field diffraction pattern. This, however, is the most insensitive position for estimating the phase error in one of the waveguides, as tracking small changes in the main lobe position is quite difficult in the presence of noise associated with phosphorous coated CCD cameras. Instead, we tune the laser until both waveguides are π out of phase. In this case, the far field radiation pattern is of two equal lobes (residing within the waveguide radiation pattern), see Fig. 4(a). Small phase errors result in one lobe increasing and the other decreasing, and we can tune the laser to the wavelength at which the lobes are equal (see Fig. 4(b)).

The wavelength identified, λ_{eq} , is now a measure of the waveguide phase error. Let us assume there is a phase error, θ_{err} , in the waveguide. Hence the phase difference between two waveguides at the design wavelength, λ_0 , is characterized by

$$k(\lambda_0) \Delta L = 2\pi m + \theta_{err}. \quad (1)$$

When we tune the laser source to identify the wavelength that results in the two waveguides being π out of phase, we satisfy

$$k(\lambda_{eq}) \Delta L = 2\pi m - \pi. \quad (2)$$

Taking the difference of Eqs. (1) and (2) and approximating the wavevector difference by the product of the wavevector derivative and the wavelength shift, we obtain

$$[k(\lambda_{eq}) - k(\lambda_0)] \Delta L \approx \frac{dk}{d\lambda} \cdot (\lambda_{eq} - \lambda_0) \Delta L = -\pi - \theta_{err}. \quad (3)$$

Using the definition for the WGR's FSR we can simplify Eq. (3) and obtain a direct measure of the phase error:

$$\theta_{err} = 2\pi \frac{\lambda_{eq} - \lambda_0}{\Delta\lambda_{FSR}} - \pi. \quad (4)$$

We now see that the phase error is linear with the deviation of λ_{eq} from the WGR's designed center wavelength. Note that we cannot distinguish errors of multiple orders of 2π . However, the technique sets the right phase for the design wavelength, λ_0 , regardless of the erroneous order. Such an error will manifest itself in distant diffraction orders, when the accumulated phase is slightly off. However, this phase error on other diffraction orders scales as the ratio of the number of 2π cycle slips (error) to the designed diffraction order, m . Since $m = 7480$ in our case, we are insensitive to multiple orders of 2π cycle slips, assuming they are small.

A fully automated WGR scanning and evaluation procedure has been developed, by placing the free-space optical measurement system on a moving stage. We assessed the accuracy for the measurement system with the 25 GHz FSR WGR by repeated measurements. We report an average error of 30 mrad for the entire system, larger than our previously reported figure in [16], where a similar measurement system obtained 13 mrad measurement error when the FSR was 5 THz. Our current error is larger due to switching to a WGR with a smaller FSR, as the measurement error is inversely proportional to the FSR. Also, the wavelength accuracy of the scanning laser starts to play a more dominant role in such small FSR cases.

In order to account for the two orthogonal polarizations, a polarizer was placed before the imaging and Fourier lens and a polarization scrambler on the laser source, enabling an independent measurement of each polarization. We found our WGR exhibits birefringence and weak correlation between the errors in the two polarizations (see Fig. 5), meaning a polarization diverse phase correction is required.

After measuring relative phases between all adjacent waveguides, we need to identify an optimized waveguide trimming strategy for minimum writing time. A degree of freedom at our disposal is the choice of absolute output phase, as it does not impact the WGR function. This is done by successively choosing each waveguide of the array to be the reference waveguide, and assessing the total accumulated phase that has to be inscribed to all other waveguides in order to achieve the equal phase property. The optimized strategy is the one that requires the least amount of accumulated phase writing.

To correct the phase errors introduced in fabrication we employed a phase trimming procedure applied post fabrication. The phase trimming was originally designed around the photosensitivity effect, which occurs for Ge-doped silica when photoexcited with light around 240–250 nm [17]. The photosensitivity effect is greatly enhanced when the glass matrix is in-diffused with hydrogen. We've tried to quantify this and have seen the expected great improvements in refractive index change. However, hydrogen is in-diffused at high pressure over long time; but when removing the WGR from the high pressure vessel the hydrogen quickly out-diffuses since the over-cladding is 12 μm thick only (within an hour in general). This out-diffusion time

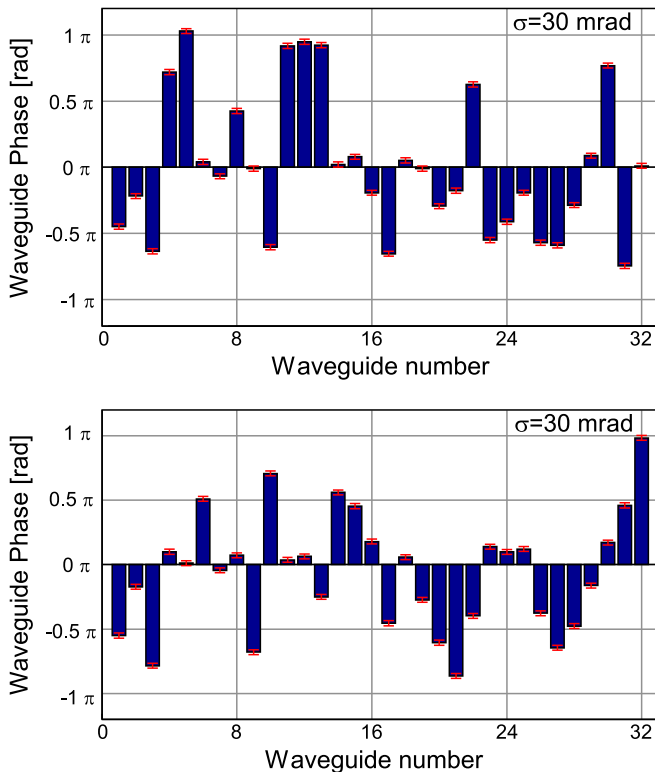


Fig. 5. Phase errors of the WGR horizontal (Top) and vertical (Bottom) polarizations.

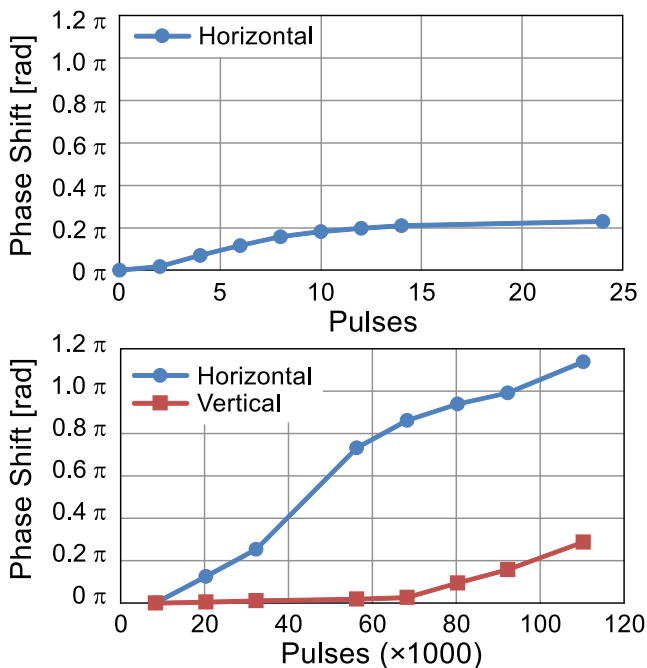


Fig. 6. Phase shift versus trim energy of a waveguide pair for photosensitivity effect (Top) and stress effect (Bottom). Photosensitivity uses a fraction of the energy needed for the same phase shift as stress, but reaches saturation after ~ 0.6 rad. Stress shows high linearity and no saturation, and phase shifts larger than the required 2π were reached (not shown).

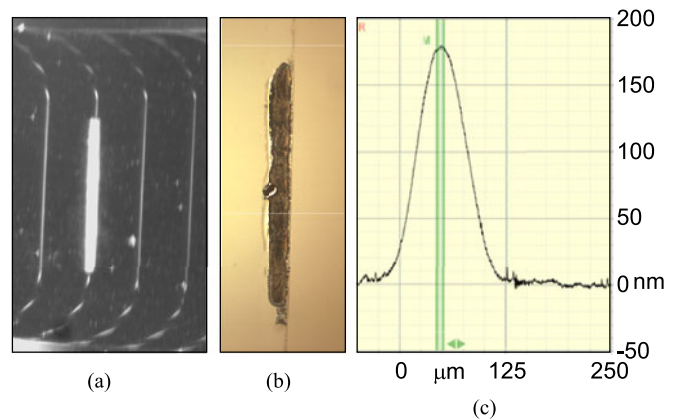


Fig. 7. Glass dilation caused by UV laser absorption in the silica cladding: (a) Camera top-view of a trimmed waveguide. The bright zone is scattered illumination light from the exposed surface; (b) microscope image of dilated spot on a clear wafer region (no waveguide underneath); (c) surface topography cross section measured along the narrow dimension of the dilated spot in (b). The formed stress gradient results in phase modulation via the photoelastic effect.

is much faster than the phase trimming time for the complete WGR, so this approach did not meet our requirements.

Without hydrogen loading the photosensitivity effect gave us only ~ 0.6 rad of phase trimming ability for our available waveguide length in the exposure zone (see Fig 6, top), whereas we require full 2π trimming range ability. However, over prolonged exposure to UV energy, the absorbed UV light in the silica glass over-cladding causes a dilation in the glass and the formation of a local positive index change resulting from the stress [18]. We confirmed the glass dilation by measuring with a Dektak stylus profiler the surface topography of an illuminated cladding area (see Fig. 7(c)). The stress in the dilated cladding above the waveguide results in very large phase delays due to the photoelastic effect (see Fig 6, bottom) [19], and provided us with the necessary phase controls. It should be noted that as the formed stress gradient results in different delays for each polarization (see Fig 6, bottom), this solution requires a polarization diversity arrangement. We trimmed with laser pulses from an KrF excimer laser (248 nm), focused on the individual waveguides with a cylindrical and through a metal mask with a rectangular aperture. Waveguide targeting was aided by an overhead camera monitoring system.

Unlike photosensitivity, stress induced phase shifts undergo stress relaxation (see Fig. 8). We identified two stress relaxation mechanisms impacting the inscribed stress field, one which occurs immediately after the PLC mounting vacuum is released, and another related to relaxation in the glass over time. We addressed the vacuum related relaxation by bonding the PLC to a 3 mm thick Borosilicate glass buffer, for rigidity, as it also shares the same thermal expansion coefficient as the Silicon substrate.

The glass relaxation was dealt by trimming the waveguides over several cycles, until the system reached stress equilibrium. Generally three writing cycles were required, with a waiting time of two weeks in between. Thermal annealing may expedite this wait time. Fig. 8 shows the measured WGR phase errors for the design wavelength before and after initial phase

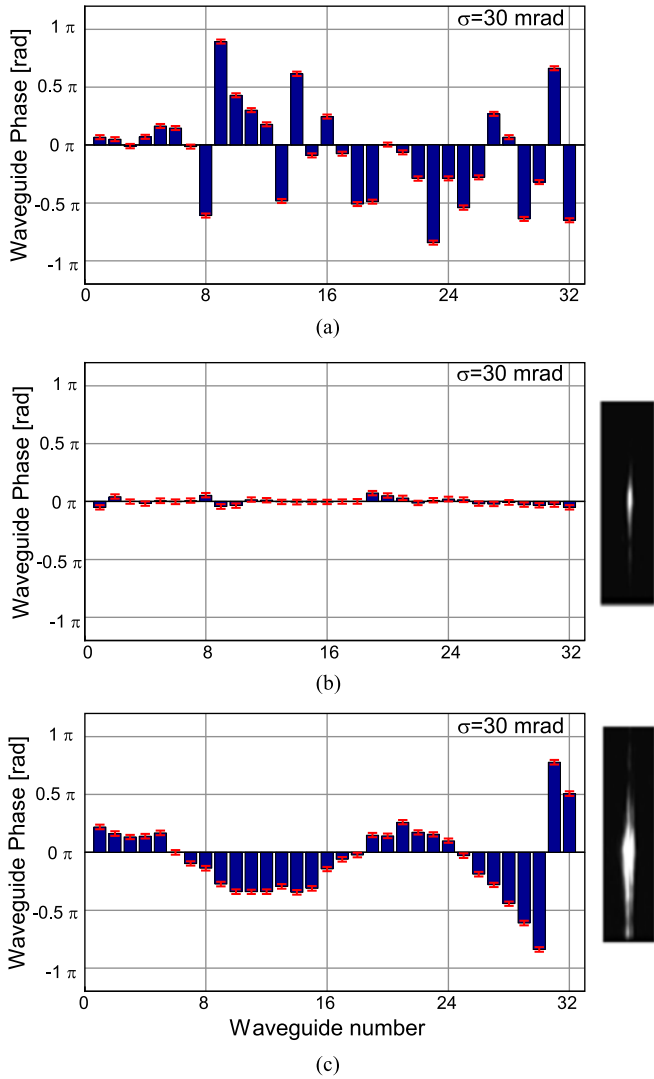


Fig. 8. Phase errors of the WGR: (a) before trimming, (b) after trimming, and (c) after two weeks and stress relaxation. The effect of stress relaxation is shown by phase measurements as well as Fourier plane pictures taken right after the trimming (b) and two weeks later (c).

trimming, and after a two week relaxation period. What starts out as almost random (though very stable) phase values with no relative relationship, are brought to the same target value. Even though the phase trimming is not perfect, the performance is good enough to have fine spectral selectivity in the Fourier plane, and no degradation has been observed over several months after repeating the trimming process three times.

IV. PHOTONIC SPECTRAL SYSTEM FOR FINE RESOLUTION FILTERING

We assembled the filtering setup and prescribed different filtering functions with the LCoS SLM. This is done by placing the LCoS SLM at the Fourier plane of the WGR and reflecting the modulated light back to the WGR and output fiber. The SLM was placed at a slight tilt diverting all light out the optical path (to eliminate the cover glass back reflection and the second polarization). A linear phase ramp function was written on the

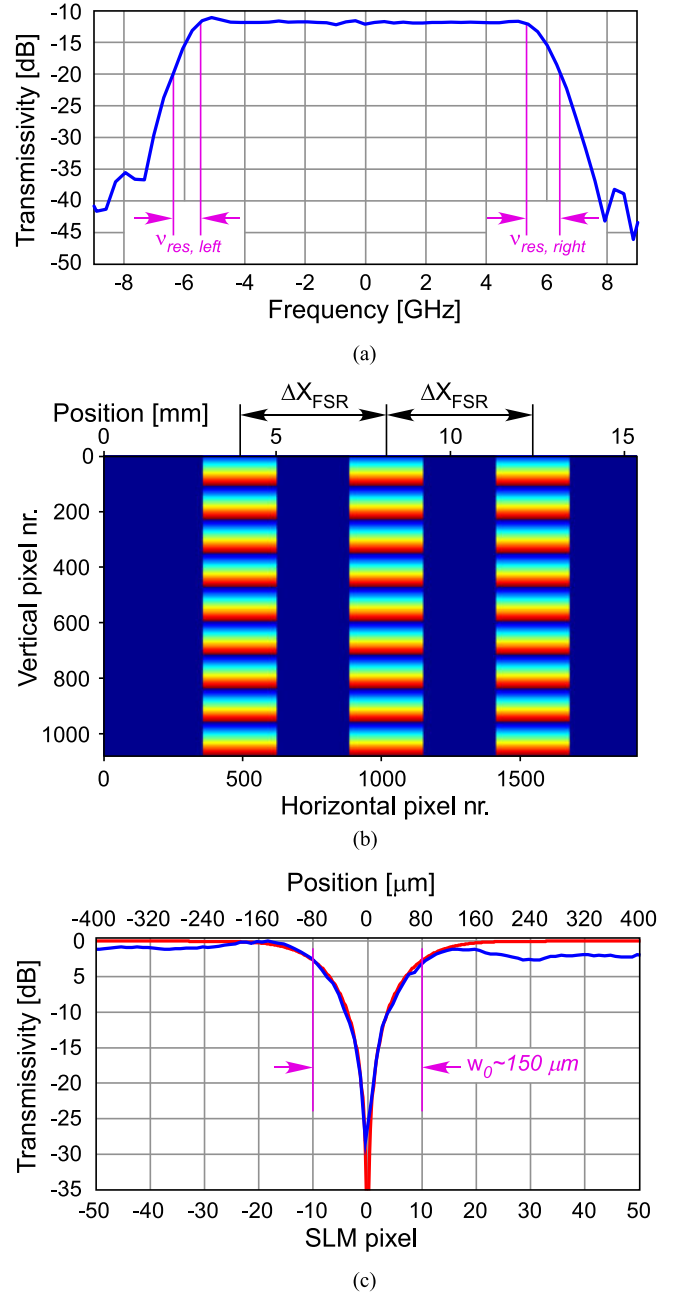


Fig. 9. (a) Resolution metrics of ~ 1 GHz measured from -0.5 dB (90%) down to -10 dB (10%). (b) Phase function written to the SLM, for selecting 12.5 GHz band, including higher order diffraction orders. (c) Spot size measurement ($2w_0 \sim 300 \mu\text{m}$), by scanning a 0-Pi phase transition across the monochromatic spot with the LCoS modulator (Gaussian model fit in red).

SLM in order to steer back selected spectral components with desired attenuation and phase. Since each spectral component radiating into free space from the waveguide array excites few diffraction orders, we back reflect them all to collect all the energy. This is done by repeating the frequency selection pattern on the SLM with offsets corresponding to the WGR diffraction orders that are spatially offset by ΔX_{FSR} (see Fig. 9(b)). Selecting a frequency band in this manner achieves uniform performance no matter where the frequency band occurs with respect to the center frequency of the WGR.

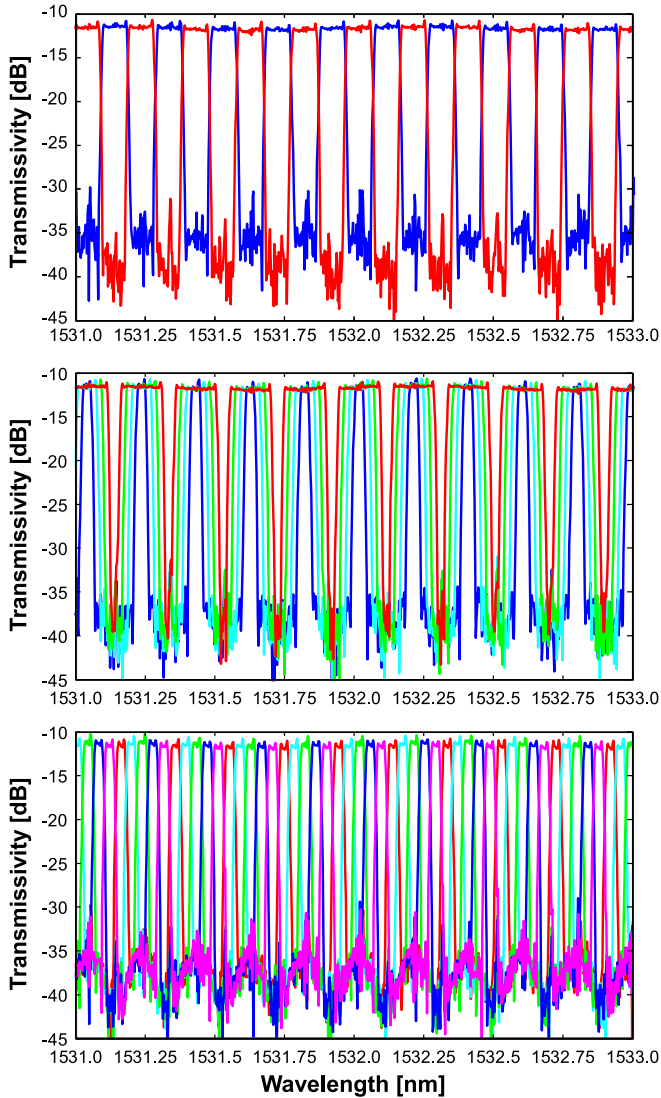


Fig. 10. Top: Selection of 12.5 GHz wide passband, on and off grid, for quasi 12.5/25 GHz interleaver functionality. Center: Flexible selection of bandwidth: 5, 10, 15, and 20 GHz wide passbands on grid. Bottom: Selection of 5 GHz wide passbands across the 25 GHz FSR.

Any bandwidth selection can be prescribed by appropriate control of the SLM. We study the passband features using a swept laser technique, as grating based optical spectrum analyzers do not have sufficient spectral resolution. The passband edge assessments show that the 90%–10% transitions occur at 1.3 GHz resolution on one side and 0.9 GHz resolution on the other side, indicating that the spot size is slightly asymmetric (see Fig. 9(a)). Nevertheless, the optical filtering performance is extremely sharp and suitable for the OFDM-PON application [15] which calls for transitions from pass to block bandwidth of 3.125 GHz. We apply the interleaver functionality and block out 12.5 GHz slices as well as flexible bandwidth carving and center wavelength selection (see Fig. 10).

In addition to the resolution metric, a PSP is also characterized by the positional accuracy at which it is possible to encode a spectral function on the LCoS SLM. This positional accuracy is defined as the spectral addressability. Knowing the

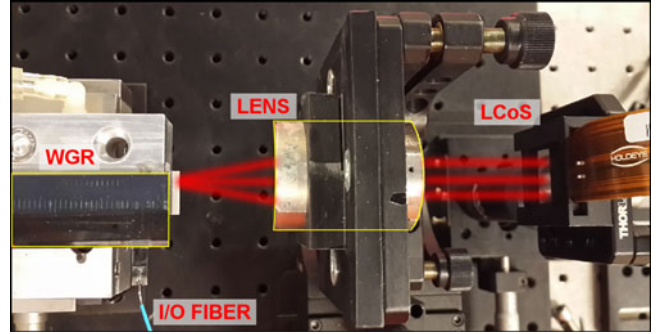


Fig. 11. PSP set-up consisting of WGR, Fourier lens, and LCoS SLM only.

spatial dispersion term $dx/d\nu$ and LCoS pixel size p , the spectral addressability is $p/(dx/d\nu)$. In our PSP implementation the LCoS pixel size is $8\ \mu\text{m}$ (Holoeye Pluto, 1920×1080 pixels) and the spatial dispersion equals $160\ \mu\text{m}/\text{GHz}$, yielding record ~ 50 MHz addressability for our PSP.

A spot size of $2w_0 \approx 300\ \mu\text{m}$ was measured by scanning a $0\text{--}\pi$ abrupt spatial phase jump through the spot in the dispersion direction when excited with a CW laser using the SLM and monitoring the fiber coupled power (see Fig. 9(c)). Details of this spot size measurement technique provided in the Appendix. Using this in the PSP resolution definition we get $\Delta\nu_{res} = w_0/(dx/d\nu) \approx 1$ GHz, in agreement with our direct resolution measurement.

The observed loss in this setup (see Fig. 11) is -12 dB. The identified loss mechanisms are as follows: WGR fiber coupling efficiency ($\times 2$) -6.5 dB, and LCoS SLM reflectivity -2 dB. The total known loss amounts to -8.5 dB, leaving unaccounted losses of 3.5 dB that are likely from inefficiency of optical collimation and focusing back to WGR. We noticed that the insertion loss of the WGR increased by 0.7 dB after the trimming process, from -2.5 to -3.2 dB. This might be due to light scattering from the dilated waveguide cladding.

V. CONCLUSION

In this paper we introduced a fine resolution PSP, built upon a 25 GHz WGR that underwent permanent phase error corrections via a UV excimer laser. The optical filtering arrangement is greatly simplified thanks to the phase-corrected WGR, and is compact and robust. The PSP's spectral filtering ability was provided by an LCoS SLM in the Fourier plane, enabling us to create a 12.5/25 GHz interleaver, and a flexible selection of filter realizations, with 1 GHz optical resolution and 50 MHz spectral addressability. Due to polarization dependent errors and trimming, this error correction method requires polarization diversity. In addition, the amount of trimming repetitions needed for this correction method makes it more feasible for WGRs with small number of waveguide arms.

APPENDIX

In this Appendix we discuss the beam size measurement technique we employ with a phase SLM in the spectral plane. When a CW beam impinges on the spectral plane, we can experimentally

assess its size by scanning a $0\text{-}\pi$ phase transition across the beam and plot the reflected fiber-coupled power. Assuming the beam is Gaussian shaped, its field (in one dimension) is defined by

$$G(x) = \left(\frac{2}{\pi w_0^2}\right)^{1/4} \exp\left(-\frac{x^2}{w_0^2}\right). \quad (\text{A1})$$

The Gaussian beam defined in Eq. (A1) is normalized such that its power coupling is unity. We calculate the fiber power coupling integral when part of the beam is at phase zero, and the complementary part at π phase (or negative), yielding

$$|\eta|^2 = \left(\int_{-\infty}^{\xi} G^2(x) dx - \int_{\xi}^{\infty} G^2(x) dx\right)^2 = \text{erf}^2\left(\frac{\sqrt{2}\xi}{w_0}\right). \quad (\text{A2})$$

Obviously Eq. (A2) yields zero fiber coupled power at $\xi = 0$ (centered on the beam) due to destructive interference between the two halves (which is useful for identifying the beam position), and unity at $\xi = \pm\infty$. To assess the beam radius, w_0 , we seek the fiber coupled power at $\xi = \pm w_0/2$, which is $|\eta|^2 = 0.466$ or -3.3 dB. The full width at -3.3 dB level is easy to experimentally measure and provides the value of w_0 , out of which the full beam size, $2w_0$, is obtained. This measurement and an experimental fit to Eq. (A2) is depicted in Fig. 9(c).

REFERENCES

- [1] D. M. Marom *et al.*, "Wavelength-selective 1×2 switch utilizing a planar lightwave circuit stack and a MEMS micromirror array," presented at the Optical MEMS, Takamatsu, Japan, Aug. 2004.
- [2] T. Ducellier *et al.*, "Novel high performance hybrid waveguide-MEMS 1×9 wavelength selective switch in a 32-cascade loop experiment," presented at the Eur. Conf. Optical Communication, Stockholm, Sweden, 2004, Paper Th4.2.2.
- [3] N. Ooba *et al.*, "Compact wide-band wavelength blocker utilizing novel hybrid AWG-free space focusing optics," presented at the Optical Fiber Communication Conf., San Diego, CA, USA, 2008, Paper OWI2.
- [4] D. Sinefeld and D. M. Marom, "Spectral processor implemented with hybrid free-space and guided-wave optics and active LCoS modulator," in *Proc. IEEE 25th Conv. Electr. Electron. Eng. Israel*, Eilat, Israel, 2008, pp. 380–383.
- [5] J. E. Ford, V. A. Aksyuk, D. J. Bishop, and J. A. Walker, "Wavelength add-drop switching using tilting micromirrors," *J. Lightw. Technol.*, vol. 17, no. 5, pp. 904–911, May 1999.
- [6] D. M. Marom, D. T. Neilson, D. S. Greywall, P. Chien-Shing, N. R. Basavanthally, V. A. Aksyuk, D. O. Lopez, F. Pardo, M. E. Simon, Y. Low, P. Kolodner, and C. A. Bolle, "Wavelength-selective $1 \times K$ Switches using free-space optics and MEMS micromirrors: Theory, design, and implementation," *IEEE J. Lightw. Technol.*, vol. 23, no. 4, pp. 1620–1630, Apr. 2005.
- [7] D. Sinefeld and D. M. Marom, "Hybrid guided-wave/free-space optics photonic spectral processor based on LCoS phase only modulator," *IEEE Photon. Technol. Lett.*, vol. 22, no. 7, pp. 510–512, May 2010.
- [8] K. Seno, K. Suzuki, N. Ooba, T. Watanabe, M. Itoh, S. Mino, and T. Sakamoto, "50-wavelength channel-by-channel tunable optical dispersion compensator using a combination of AWG and bulk grating," *IEEE Photon. Technol. Lett.*, vol. 22, no. 22, pp. 1659–1661, Nov. 2010.
- [9] D. Sinefeld, C. R. Doerr, and D. M. Marom, "A photonic spectral processor employing two-dimensional WDM channel separation and a phase LCoS modulator," *Opt. Exp.*, vol. 19, pp. 14532–14541, 2011.
- [10] T. Kamalakis, T. Sphicopoulos, and D. Syvridis, "An estimation of performance degradation due to fabrication errors in AWGs," *J. Lightw. Technol.*, vol. 20, no. 9, pp. 1779–1787, Sep. 2002.
- [11] K. Takada, Y. Inoue, H. Yamada, and M. Horiguchi, "Measurement of phase error distributions in silica abased arrayed-waveguide grating multiplexers by using Fourier transform spectroscopy," *Electron. Lett.*, vol. 30, pp. 1671–1672, 1994.
- [12] K. Takada, M. Abe, T. Shibata, and K. Okamoto, "1-GHz-spaced 16-channel arrayed-waveguide grating for a wavelength reference standard in DWDM network systems," *J. Lightw. Technol.*, vol. 20, no. 5, pp. 850–853, May 2002.
- [13] R. Rudnick *et al.*, "Sub-banded/single-sub-carrier drop-demux and flexible spectral shaping with a fine resolution photonic processor," presented at the Eur. Conf. Optical Communications, Cannes, France, 2014, Paper PD.4.1.
- [14] N. Goldshtein, L. Pascar, D. Sinefeld, O. Golani, and D. M. Marom, "Fine resolution spectral filtering using a 25GHz free-spectral range arrayed waveguide grating," presented at the Optical Fiber Communication Conf., Los Angeles, CA, USA, 2015.
- [15] A. Agmon *et al.*, "OFDM/WDM PON with laserless, colorless 1 Gb/s ONUs based on Si-PIC and slow IC," *J. Opt. Commun. Netw.*, vol. 6, no. 3, pp. 225–237, 2014.
- [16] D. Sinefeld, N. Goldshtein, R. Zektzer, N. Gorbato, M. Tur, and D. M. Marom, "Output radiating waveguide grating router: Characterization of phase errors and UV trimming," presented at the Bragg Gratings, Photosensitivity, Poling Glass Waveguides, Colorado Springs, CO, USA, Jun. 2012.
- [17] D. L. Williams *et al.*, "Direct observation of UV induced bleaching of 240nm absorption band in photosensitive germanosilicate glass fibres," *J. Electron. Lett.*, vol. 28, no. 4, pp. 369–371, 1992.
- [18] H. N. J. Fernando, J. Canning, L. Wosinski, B. Jaskorzynska, and M. Dainese, "Characterization of ultra-violet-induced changes in planar waveguides," *J. Opt. A, Pure Appl. Opt.*, vol. 5, pp. 335–340, 2003.
- [19] F. Kherbouche *et al.*, "UV-induced stress field during Bragg grating inscription in optical fibres," *J. Opt. A, Pure Appl. Opt.*, vol. 3, pp. 429–439, 2001.

Authors' biographies not available at the time of publication.